

# Simulated Structural and Electronic Properties of Cation-Disordered ZnGeN<sub>2</sub> and its Interface with GaN

Jacob J. Cordell<sup>1,2,\*</sup> Moira K. Miller<sup>1,2</sup> M. Brooks Tellekamp<sup>1,2</sup> Adele Tamboli<sup>1,2</sup>  
Garrett J. Tucker<sup>1</sup> and Stephan Lany<sup>2,†</sup>

<sup>1</sup>*Department of Mechanical Engineering, Colorado School of Mines, Golden, Colorado 80401, USA*

<sup>2</sup>*Materials Science Center, National Renewable Energy Laboratory, Golden, Colorado 80401, USA*

<sup>3</sup>*Department of Physics, Colorado School of Mines, Golden, Colorado 80401, USA*



(Received 5 July 2022; revised 17 October 2022; accepted 18 October 2022; published 12 December 2022)

Cation disorder is increasingly being studied as a means of tuning properties in electronic materials. Through Monte Carlo simulations and first-principles calculations, we determine the ranges of elastic moduli and polarization constants in ZnGeN<sub>2</sub> as a function of ordering. We use heterostructure calculations to demonstrate a disorder-dependent type-I or type-II band offset between relaxed GaN and strained ZnGeN<sub>2</sub> in the polar [001] direction. Modeling polarization and band offsets, we then use these calculations to comment on which values are desirable for device design, which parameters are obtainable through targeted growth techniques, and the challenges that remain in realizing a device and understanding cation disorder in heterostructures. Although the elastic and polarization properties change little with the order parameter, the band characteristics undergo dramatic shifts, creating a type-I band offset in partially disordered material.

DOI: 10.1103/PhysRevApplied.18.064030

## I. INTRODUCTION

A variety of ternary nitrides are currently explored for the use of their site disorder and their relevance to present electronics, which rely on the more thoroughly researched binary nitrides [1–7]. The small lattice mismatch (< 1%) between ZnGeN<sub>2</sub> and GaN and the similar band gaps of the two materials (3.6 eV for ZnGeN<sub>2</sub> versus 3.5 eV in GaN) make ZnGeN<sub>2</sub> a candidate for quantum well based optoelectronics, namely light-emitting diodes (LEDs) [8–10]. Cation disorder in ZnGeN<sub>2</sub> has been shown to reduce the band gap of the system into and below the green and amber region of emission specifically desired for manufacturing inorganic color-mixed LEDs [11–13]. The lack of emitters between current efficient nitride and phosphide visible light emitters has been deemed the “green gap” and creates a barrier to implementing highly efficient solid-state lighting. ZnGeN<sub>2</sub> quantum wells present a pathway

to achieve higher efficiencies but grown materials exhibit a wide range of ordering and the impact of this ordering on device properties is not yet clear [14,15]. In this study, we use computationally generated structures of ZnGeN<sub>2</sub> to calculate the sensitivity of device parameters to cation ordering.

One of the most crucial elements for determining the properties and design of electronic devices is the electronic band character at the interfaces of the device. ZnGeN<sub>2</sub> has gained special interest for its wide tunable band gap. However, the same cation ordering to which the bulk band gap of ZnGeN<sub>2</sub> is so sensitive also alters the interfacial band offsets between ZnGeN<sub>2</sub> and GaN, including the type of offset. In a type-I (straddling) offset, the band gap of one material falls entirely within the energy gap of the other material, as shown schematically in Fig. 1. In type II (staggered), the valence-band maximum (VBM) and conduction-band minimum (CBM) of each material are offset in the same direction (positive or negative) with respect to the band extrema of the other material and in a type-III (broken) offset, the CBM of one material is below the VBM of the other, creating band overlap, which poses no barrier to conduction at the interface. The type-II offset is seen as ideal for forcing recombination at the interface of polar materials by promoting strong overlap of carrier wave functions driven by strong polarization fields that act to separate carriers in type-I quantum wells, an effect known as the quantum confined Stark effect. The

\*cordell@mines.edu

†stephan.lany@nrel.gov

Published by the American Physical Society under the terms of the [Creative Commons Attribution 4.0 International license](#). Further distribution of this work must maintain attribution to the author(s) and the published article's title, journal citation, and DOI. Open access publication funded by the National Renewable Energy Laboratory (NREL) Library, part of a national laboratory of the U.S. Department of Energy.

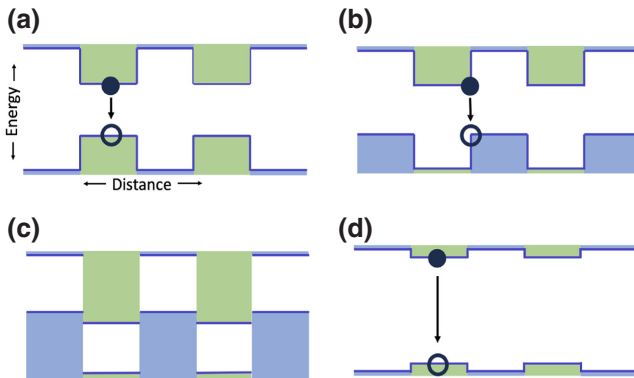


FIG. 1. Types of band offsets: (a) type I, straddling; (b) type II, staggered; (c) type III, broken; and (d) nearly even band edges. The closed and open circles represent electrons and holes, respectively, and where they likely recombine.

recombination energy is dictated by the difference between the higher VBM and lower CBM, which in the case of the type-II offset fall in two separate materials.

The current literature lacks consensus on the band offsets between ordered ZnGeN<sub>2</sub> and GaN due to significant differences in the structures used, the crystallographic orientations measured, and the calculation methods followed [16–21]. To date, four main sets of calculations exist predicting the band offsets between these materials. Jaroenjittichai *et al.* use the linearized muffin-tin orbital approach with a *GW* correction in the ZnGeN<sub>2</sub>/GaN heterostructure [16,17]. They use the wurtzite-derived structures for each material to calculate offsets in the nonpolar [100] and [010] directions as well as the polar [001] direction and then remove the strain contribution to the potential alignment to develop a direction-independent prediction of the natural offset. The ZnGeN<sub>2</sub>/GaN valence-band offset  $\Delta E_v$  is calculated in their work as 1.24 eV for [001] and 1.1 eV for the natural offset. These simulations seem to agree with recent VBM positions calculated from XPS spectra of films grown with metal-organic chemical-vapor deposition (MOCVD) [21]; however, questions remain in this comparison as to the degree of cation order in the ZnGeN<sub>2</sub> grown, which dictates the magnitude of the band gap [11,13] as well as the position of the Fermi level in these heterostructures, thereby convoluting the interpretation of the valence-band offsets.

The method of Ref. [16] has later been extended by Lyu *et al.* with further consideration of the dipole formation at this interface to develop more accurate natural offsets of  $\Delta E_v = 0.49$  eV [18]. Other calculations rely on the comparison of bulk calculations aligned via the vacuum potential or potential level of a H interstitial to determine band offsets. Cao *et al.* have calculated the offset between cubic ZnGeN<sub>2</sub> and GaN in the polar [001] direction aligned using the vacuum level of, presumably,

their respective chalcopyritelike and zincblendelike structures,  $\Delta E_v = 0.38$  eV, although these structures are not explicitly stated [19]. Adamski *et al.* have chosen the nonpolar [1100] GaN and [100] ZnGeN<sub>2</sub> directions for their calculations in the wurtzite-derived structures and have found offsets in the opposite direction from Ref. [16] both in aligning the vacuum levels of the bulk structures,  $\Delta E_v = -0.28$  eV, and separately the H interstitial levels of ZnGeN<sub>2</sub> and GaN,  $\Delta E_v = -0.40$  eV [20]. These previous studies are each applicable to different growth scenarios but are not immediately comparable to each other or the present study without the context above to highlight the differences in approach. Here, we provide calculations of the polar [001] interface of ZnGeN<sub>2</sub>/GaN in the ground-state wurtzite-derived structures by calculating the local potential from density-functional theory (DFT). We use a hybrid functional to accurately reproduce the band positions of the heterostructure.

In this study, we model band offsets and interface-relevant properties for ZnGeN<sub>2</sub> structures with varying degrees of order to inform the design of ZnGeN<sub>2</sub>/GaN-heterostructure devices based on the role of cation ordering. We use the Bragg-Williams long-range-order (LRO) parameter  $S$  to quantify site order [22,23]:  $S = r_\alpha + r_\beta - 1$ , where  $r_\alpha$  is the fraction of site  $\alpha$  occupied by atom  $\alpha$  and  $r_\beta$  is the fraction of site  $\beta$  occupied by atom  $\beta$ . In stoichiometric material as is studied here,  $r_\alpha = r_\beta$ . Cations are swapped via Monte Carlo simulation to obtain realistic structures with varied LRO parameters [24]. These structures are then relaxed using DFT to obtain elastic moduli, piezoelectric constants, dielectric constants, and spontaneous polarization. The site disorder pertains to the ordering of ions on their set crystallographic sublattice, which can be measured at short range as the nitrogen coordination environment or long range as the overall adherence to the ground-state structure. In this work, we integrate prior Monte Carlo simulations explained in Ref. [24] and electronic structure calculations from Ref. [13]. In addition to coefficients to be used in higher-level device modeling, we also model the band offsets of ZnGeN<sub>2</sub> and GaN, taking each in turn as the substrate and epitaxial film layers. Band offsets are calculated for disordered ZnGeN<sub>2</sub> strained to GaN substrates to a level attainable with DFT and available computing resources for relatively large cells.

## II. BAND OFFSETS

The band offsets between two materials determine the direction of carrier movement and the height of potential barriers preventing movement of carriers in specific directions across interfaces. Between ZnGeN<sub>2</sub> and GaN, the literature, ranging from patents on using the heterostructure in a device [8] to calculations [16,17,19,20] and recent experimental measurements [21,25], establishes these barrier heights and offsets. All present calculations in the

literature focus on cation-ordered ZnGeN<sub>2</sub>, which is not necessarily the configuration of material grown either by MOCVD [12,21,26] or molecular-beam epitaxy (MBE) [25,27]. The ordered calculations all predict a type-II offset but disagree on the direction of the offset, largely due to different modeling of growth as either epitaxial or nonoriented. Synthesis methods used for growing ZnGeN<sub>2</sub> with a substrate other than GaN in fact highlight the difficulty of obtaining ordered ZnGeN<sub>2</sub> films [14,15,28,29]. Reference [20] addresses the disagreement in the literature around the direction and magnitude of offsets between ordered ZnGeN<sub>2</sub> and GaN based on the different methods used to calculate these parameters. The calculations represented in this section are performed at the DFT level for interface structures. *GW* and single-shot hybrid functional calculations are used for GaN and ZnGeN<sub>2</sub> bulk structures (see Sec. VIB 2).

### A. Ordered ZnGeN<sub>2</sub>

The band offsets in Fig. 2 show the narrowing of both the ZnGeN<sub>2</sub> and GaN band gaps by roughly 0.2 eV when each is strained anisotropically to the other using the orthorhombic lattice parameters  $a = 6.426 \text{ \AA}$  and  $b = 5.565 \text{ \AA}$  for GaN and  $a = 6.399 \text{ \AA}$  and  $b = 5.542 \text{ \AA}$  for ZnGeN<sub>2</sub>. The slope in the bands is calculated from the change in average potential across each material for a periodic interface of the two materials visualized above each band-offset plot. The offset in energy between the ZnGeN<sub>2</sub> and GaN conduction bands is small when ZnGeN<sub>2</sub> is strained to GaN, within error of having no offset step in energy. In the case of a GaN quantum well, the conduction-band offset is indeed calculated to be negligible in [001] and the valence band of

strained GaN is slightly raised with respect to the relaxed ZnGeN<sub>2</sub> valence band.

The small difference in valence-band position between ZnGeN<sub>2</sub> and GaN using either material as the relaxed substrate lies in between previous predictions alternately indicating either a higher ZnGeN<sub>2</sub> band position [17,18] or a higher GaN band position [20]. Our results for the ordered structure most closely resemble those of Ref. [20], who use a similar hybrid functional suggesting (as they discuss) that the careful choice of functional used in calculations plays a significant role in the offset prediction. Furthermore, for disordered ZnGeN<sub>2</sub>, we observe significant changes not only in the direction and magnitude of the band offsets but also the type of alignment from type II to type I.

The present band-offset results for ordered ZnGeN<sub>2</sub> between layers of GaN do not create a strong argument for use as a quantum well because the barrier heights for electron and hole conduction are not substantial enough to block electrons and holes and direct recombination at the interface. While a quantity that dictates the necessary degree of confinement is not well defined, prior studies in Al<sub>x</sub>In<sub>1-x</sub>P suggest that 80-meV offsets do not block carriers from tunneling, while confinement of 150 meV or more proves sufficient [30]. Even assuming that carriers do recombine at the interface, the small barrier heights barely reduce the recombination energy, meaning that any photons emitted are predicted to be  $> 3 \text{ eV}$ , higher in energy than the visible spectrum and much higher than the target wavelengths of 2.1 eV and 2.3 eV for amber and green emission. Additional electron- and hole-blocking layers are common in current device designs for LEDs and would need to be implemented in the case of an ordered ZnGeN<sub>2</sub>.

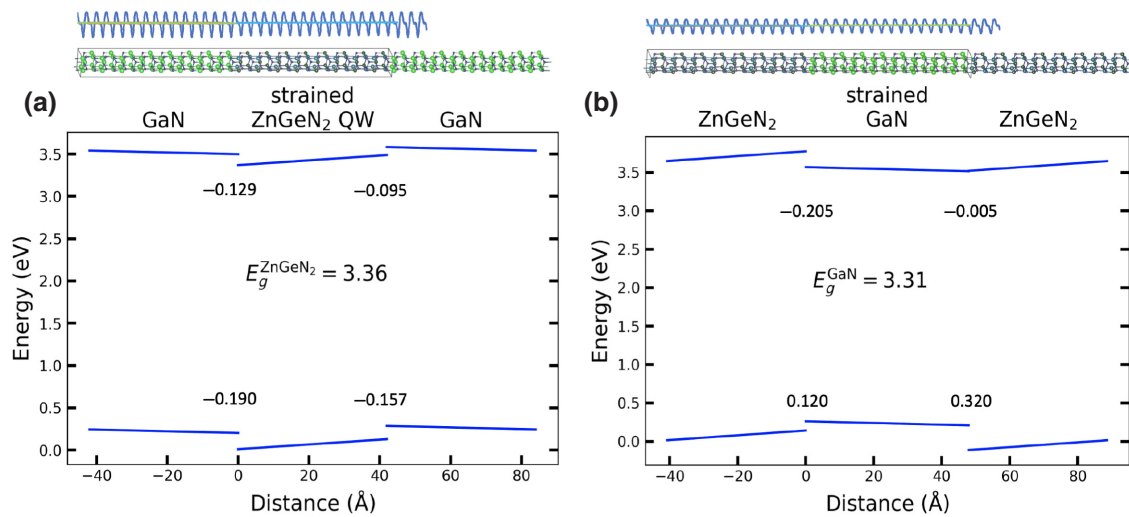


FIG. 2. Band offsets for (a) ZnGeN<sub>2</sub> strained to GaN and (b) GaN strained to ZnGeN<sub>2</sub>. Each offset is labeled with the energy difference from substrate to film and band gaps are labeled for films under strain. The quantum well structure, a section of which is shown above each energy offset along with the averaged oscillating potential of the heterostructures, is periodic.

active layer to consistently stop carriers from hopping over the small offsets shown in Fig. 2.

## B. Disordered ZnGeN<sub>2</sub>

Because cation disorder reduces the band gap of ZnGeN<sub>2</sub>, the offsets in band edges between ZnGeN<sub>2</sub> and GaN are likewise affected. In the ordered material, the similar band gaps of the two materials and the minimal offset in the electric potentials results in a small type-II offset where the ZnGeN<sub>2</sub> VBM and CBM lie less than 200 meV below the GaN band edges. Introducing a single defect pair (a concentration of  $1.7 \times 10^{20} \text{ cm}^{-3}$  or 0.39% of possible states), however, immediately raises the VBM dramatically and negligibly lowers the CBM so that a type-I offset is realized. As further site disorder is introduced, this type-I offset becomes more apparent as the VBM continues to increase significantly and the CBM decreases weakly with a decreasing order parameter. Figure 3 shows three examples of band offsets with ZnGeN<sub>2</sub> strained to GaN, where  $S$  indicates the long-range-order parameter.

The change in the type of band offset in configurations with  $0.9 \leq S < 1$  depends on the definition of the band gap, which in prior discussion we take to be the difference in energy of the highest occupied and lowest unoccupied states. In computationally generated cells, this interpretation of the band gap is not immediately distinguishable

from a wider gap with occupied defect states, as seen in Fig. 3(b). If we accept the isolated states above the valence band as defect states rather than valence-band continuum states, then the offset remains type II for higher order parameters, albeit with some localized midgap states. Further discussion on interpretation of band-gap energies can be found in Ref. [13], where the inverse participation ratio (IPR) is used to distinguish localized and potentially defect states from the band continua. The IPR is a measure of carrier localization and is calculated as  $\text{IPR}(E) = N_A \sum_i p_i(E)^2 / [\sum_i p_i(E)]^2$ , where  $N_A$  is the number of atoms in a supercell.  $p_i(E)$  is the local density of states (LDOS) projected on atom  $i$  as a function of energy  $E$ . The raised VBM states in Fig. 3(b) are highly localized, with IPRs of 100–200 compared to IPRs all less than 2 in the fully ordered system, suggesting that band gaps may not be as narrow as they appear when not accounting for IPR.

In Fig. 3, the density of states calculated for each configuration is superimposed on the band offset by aligning the appropriate band edges taken from hybrid calculations described in Sec. VI B 2. The structure corresponding to Fig. 3(a) is the ordered structure. The structure for Fig. 3(b) contains one exchange defect ( $\text{Zn}_{\text{Ge}} + \text{Ge}_{\text{Zn}}$ ) and demonstrates how the highest occupied state is raised but separates from the valence-band continuum, creating three distinct defect states, while the valence-band edge and conduction-band edge remain almost unchanged.

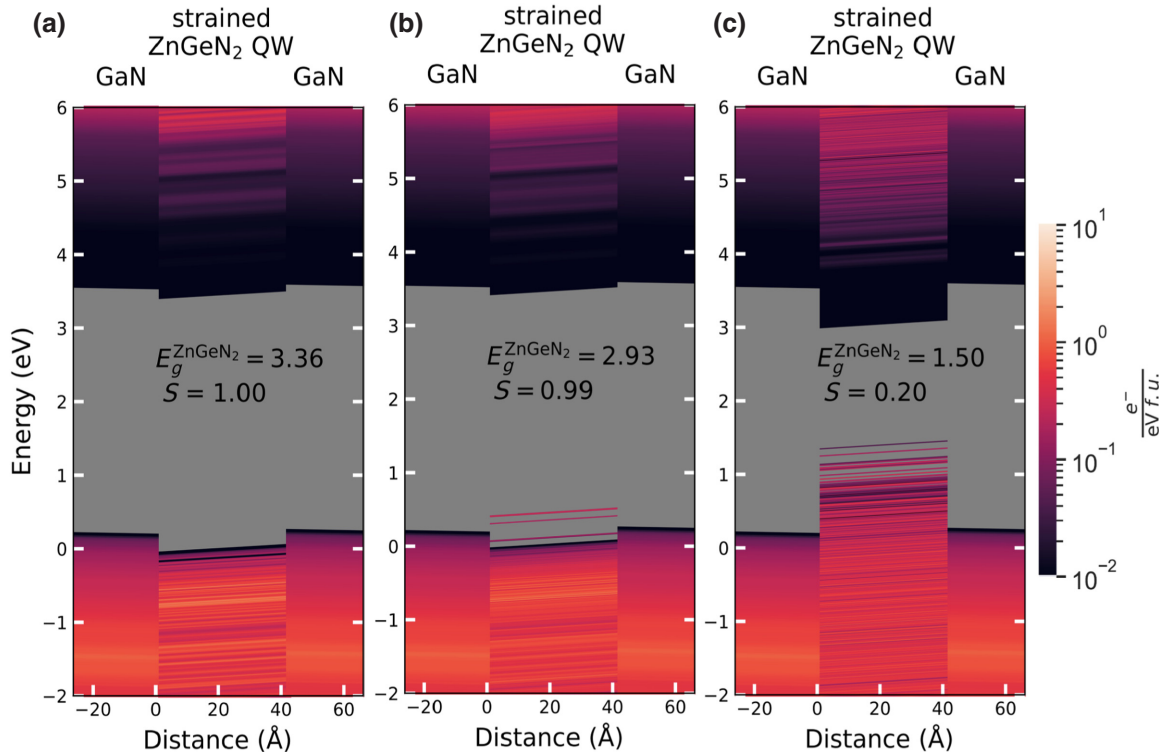


FIG. 3. Band offsets for three instances of ZnGeN<sub>2</sub> with a varied long-range-order parameter strained to GaN. The color bar indicates the density of states, while the gray areas indicate forbidden gaps. f.u. represents the formula unit for each compound.

Figure 3(b) represents a dilute, native-defect case. When the material is mostly disordered as in Fig. 3(c), the conduction-band edge lowers and the valence-band edge rises significantly. Whereas the impact of dilute defects on type of offset is debatable, a significant degree of disorder in ZnGeN<sub>2</sub> unquestionably creates a type-I offset with GaN. Here too, defect states are introduced, but these are less separated in energy from the valence-band continuum and the previous study of inverse participation ratio in these structures shows that the defect states in the disordered samples are roughly as localized as those in the dilute-defect case [13].

Figure 4 displays the band positions of ZnGeN<sub>2</sub> structures with a larger variety of order parameters than the examples from Fig. 3. Through Fig. 4, we compare the shifts in band positions with their associated shrinking band gaps in more disordered structures. A small fraction of native defects introduces defect states and the energy level of these defects is quite variable, being more dependent on the exact configuration than on the order parameter. A gap in order parameters exists between  $S = 0.2$  and 0.9 due to the sudden onset of disorder in ZnGeN<sub>2</sub> at its transition temperature [24]. For mostly disordered but not fully random structures, the valence-band continuum rises to meet the defect level. The CBM is subsequently lowered as well, leading to small band gaps near 1 eV (even more strongly disordered structures with a closed gap [13] are not considered for the purpose of the present work).

The band positions, which change with the LRO parameter, display the wide range of band gaps tunable with order despite the accessibility of only certain ranges of order parameters. The changing band positions further confirm the change in band-offset type from type II to narrowing type I moving to lower degrees of long-range order, as can be seen by the majority of the VBM lying above the GaN reference VBM and all the CBM lying below

the GaN reference CBM. As InGaN is commonly grown on GaN for LEDs emitting at and near blue wavelengths, In<sub>x</sub>Ga<sub>1-x</sub>N reference band positions where  $x = 0.1$  are also included. As seen in Fig. 4, the band-gap reduction in InGaN mainly causes a reduced conduction-band offset. Here, the GaN and In<sub>0.1</sub>Ga<sub>0.9</sub>N band energies are taken from the National Renewable Energy Laboratory (NREL) Materials Database (NRELMatDB) [31,32], with a potential alignment for bulk In<sub>0.1</sub>Ga<sub>0.9</sub>N to GaN (for further details, see Sec. VI B 2).

### III. DEVICE PARAMETERS

Device designs for quantum well LEDs depend on a variety of optical, electronic, and structural parameters that control the band structure, carrier transport, and recombination. To aid the design of suitable device heterostructures based on site disorder in ZnGeN<sub>2</sub> active layers, a set of properties are calculated to describe the material. Some of the key parameters that determine the device characteristics are the lattice parameters, elastic moduli, piezoelectric coefficients, and spontaneous-polarization constants. Some of these properties depend greatly on site order, while others are less sensitive and therefore have little impact on device characteristics. We also include calculations of dielectric constants as they relate to the piezoelectric coefficient of the material. Table I contrasts our calculations of the device parameters listed above with those from the literature on GaN and fully ordered ZnGeN<sub>2</sub>. Our calculations largely agree with the consensus of the literature for the lattice parameters and elastic constants in both materials. Fewer prior calculations exist for the electronic properties, where there is less agreement in the current literature. The calculations in this section are performed at the DFT level, as described in Sec. VI B 3.

#### A. Ordered ZnGeN<sub>2</sub>

Limited sources are available for the direction-resolved dielectric constants of GaN and ZnGeN<sub>2</sub>, but as we use similar means of calculating the dielectric constants, it is unsurprising that our calculations closely match those of Petousis *et al.* [33]. In contrast, the literature on piezoelectric constants in both materials contains a diverse set of values in cases disagreeing in the sign (i.e., direction) of the electric fields. These calculations have been refined over decades with advances in computational resources and so we draw our closest comparisons with the most recent values from the literature in each case. For instance, some of these changes in method over time include a difference in preference of the reference structure for calculating polarization. Dreyer *et al.* outline reasoning for measuring the polarization of wurtzite-derived structures with respect to a hexagonal boron nitride (*h*-BN) structure in contrast to the historically used zinc blende (*zb*) reference [34,35].

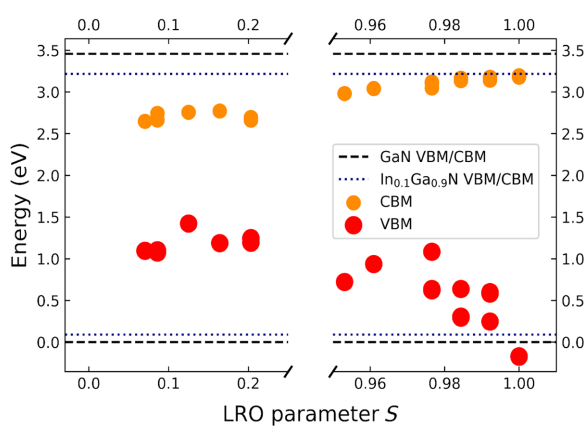


FIG. 4. Band gaps and differences in valence- and conduction-band edge positions between ZnGeN<sub>2</sub> and GaN depending on the ordering of Zn and Ge.

TABLE I. A comparison of the lattice constants, elastic moduli, piezoelectric coefficients, spontaneous polarization, and dielectric constants of GaN and ordered ZnGeN<sub>2</sub> between the present work and DFT calculations from the literature. For ZnGeN<sub>2</sub>, which takes an orthorhombic structure in its ground state,  $a_{wz}$  is taken as the average of  $a_{\text{or}}/2$  and  $b_{\text{or}}/\sqrt{3}$ , where  $a_{\text{or}} > b_{\text{or}}$ .

	GaN (present work)	GaN (literature values)	ZnGeN <sub>2</sub> (present work)	ZnGeN <sub>2</sub> (literature values)
$a_{wz}$ (Å)	3.216	3.189 to 3.216 [35,36]	3.193	3.192 to 3.215 [20,36]
$c_{wz}$ (Å)	5.239	5.185 to 5.24 [35,36]	5.203	5.2 to 5.25 [20,36]
$C_{11}$ (GPa)	323	325 to 390 [35,37,38]	299	300 to 342 [20,38,39]
$C_{22}$ (GPa)			310	291 to 358 [20,38,39]
$C_{33}$ (GPa)	357	358 to 405 [35,37,38]	346	341 to 401 [20,38,39]
$C_{44}$ (GPa)	90	90 to 105 [35,37,38]	83	85 to 103 [20,38,39]
$C_{55}$ (GPa)			91	77 to 97 [20,38,39]
$C_{66}$ (GPa)	106	107 to 123 [35,37,38]	104	87 to 97 [20,38,39]
$C_{12}$ (GPa)	111	112 to 145 [35,37,38]	109	105 to 110 [20,38,39]
$C_{13}$ (GPa)	77	78 to 106 [35,37,38]	77	76 to 138 [20,38,39]
$C_{23}$ (GPa)			72	82 to 103 [20,38,39]
$e_{15}$ (C/m <sup>2</sup> )	-0.14165	-0.139 [33]	-0.10818	-0.302 to -0.202 [20,33,39]
$e_{24}$ (C/m <sup>2</sup> )	-0.12449		-0.15341	-0.350 to -0.154 [20,33,39]
$e_{31}$ (C/m <sup>2</sup> )	-0.27140	-0.63 to 0.290 [33–35,40]	-0.2498	-0.43 to -0.300 [20,33,39]
$e_{32}$ (C/m <sup>2</sup> )			-0.24764	-0.49 to -0.290 [20,33,39]
$e_{33}$ (C/m <sup>2</sup> )	0.50156	0.465 to 1.25 [33–35,40]	0.39435	0.422 to 0.73 [20,33,39]
$P_{\text{sp}}$ (C/m <sup>2</sup> )	1.250	1.312 [34]	1.290	1.333 [20]
$\varepsilon_{11}$	10.42	10.46 [33]	10.50	10.87 [33]
$\varepsilon_{22}$			11.22	10.47 [33]
$\varepsilon_{33}$	11.55	11.65 [33]	11.62	11.51 [33]

The *h*-BN structure has the advantage of being both centrosymmetric and nonpolar, whereas the *zb* reference is noncentrosymmetric and has a nonzero formal polarization in [111]. Only recent calculations implement the *h*-BN reference for both GaN and ZnGeN<sub>2</sub>, which we also adopt here for ordered structures [20,34].

In GaN,  $C_{11} = C_{22}$ ,  $C_{13} = C_{23}$ ,  $C_{44} = C_{55}$ , and  $C_{66} = C_{11} - C_{12}/2$  due to the symmetry of its hexagonal structure. Likewise,  $e_{15} = e_{24}$ ,  $e_{31} = e_{32}$ , and  $\varepsilon_{11} = \varepsilon_{22}$ . The literature values presented along with parameters calculated for the present work highlight the breadth of current knowledge of the structure of GaN and ZnGeN<sub>2</sub>. However, consensus has not yet been reached for determining the electronic and piezoelectric properties of ZnGeN<sub>2</sub>. We follow the method of Ref. [34], using generalized gradient approximation with Hubbard  $U$  parameter (GGA+ $U$ ) calculations with the Vienna *ab initio* simulation package (VASP) [41]. The comparisons of present calculations and parameters from the previous literature provide a baseline with which to compare the effects of disorder on these same parameters. These parameters in turn control the emission profile and maximum efficiency of a ZnGeN<sub>2</sub>/GaN heterostructure used in a device.

Disordered ZnGeN<sub>2</sub> is of interest for its growth on GaN in part because of its similar lattice parameters. The similarity of the lattice parameters is confirmed in Table I, where the wurtzite equivalent of  $a$  in ZnGeN<sub>2</sub> is less than 1% removed from that of GaN. For the orthorhombic ZnGeN<sub>2</sub> structure,  $a_{wz}$  is calculated as  $a_{\text{or}}/4 + b_{\text{or}}/\sqrt{3}/2$ ,

where  $a_{\text{or}} > b_{\text{or}}$ . Likewise, the elastic constants calculated for ZnGeN<sub>2</sub> closely match those of GaN. The similarities  $C_{22} \approx C_{11}$ ,  $C_{55} \approx C_{44}$ , and  $C_{23} \approx C_{13}$  reflect the minimal basal-plane anisotropy of the orthorhombic structure of ordered ZnGeN<sub>2</sub>. Disorder further shrinks this orthorhombic distortion. The piezoelectric coefficients of ZnGeN<sub>2</sub> deviate more significantly from those of GaN, which again partly defines the practical interest in the heterostructure of the two materials.

We calculate spontaneous-polarization constants of 1.250 C/m<sup>2</sup> for GaN and 1.290 C/m<sup>2</sup> for ZnGeN<sub>2</sub>. Our calculations follow the same approach as Refs. [20,34] in predicting the spontaneous polarization, including the use of the hexagonal layered structure as a centrosymmetric reference; however, we use a different functional to relax our structures in DFT. Whereas the prior studies use the Heyd, Scuseria, and Ernzerhof (HSE) functional, we use the Perdew-Burke-Ernzerhof (PBE) approach, which results in larger lattice parameters in semiconductors than HSE [42]. The difference between these predictions can be attributed to this choice of functional.

## B. Disordered ZnGeN<sub>2</sub>

Determining the effect of site disorder in ZnGeN<sub>2</sub> on the structural and electronic properties of a ZnGeN<sub>2</sub>-GaN interface allows for making more informed decisions for designing device architecture. Predicting these impacts of disorder through computation allows us to target synthesis

pathways and potentially avoid detrimental effects from isolated defects while utilizing the potential of disorder for tuning optical band gaps. Our theoretical analysis of elastic, piezoelectric, and polarization properties of  $\text{ZnGeN}_2$  are limited to an epitaxial interface like that sought for many inorganic LEDs. Focusing on epitaxial conditions makes possible the calculation of directional piezoelectric constants corresponding to the desired axis of growth. The assumption of epitaxial interfaces also makes calculations of polarization in disordered systems possible provided that the interface remains insulating.

Modeling disorder in  $\text{ZnGeN}_2$  necessitates large supercells for Monte Carlo simulations. However, calculating elastic moduli, piezoelectric coefficients, and dielectric constants requires exponentially more time and computer memory per the quantity of atoms in the cell. Testing of different supercell sizes shows that calculating these parameters is not feasible in cells with more than 500 atoms but 128-atom cells prove workable with the available means. These 128-atom cells do not sufficiently describe order characteristics near the transition from cation order to disorder; however, they can allow us to observe the relationship between the properties listed in Table I and LRO—even at order parameters that are unlikely to be physical, as determined in prior work [24]. Additionally, although disordered  $\text{ZnGeN}_2$  is typically characterized as wurtzitelike, we choose to discuss the orthorhombic relevant parameters for properties listed in this section in order to compare with the ordered structure. This orthorhombic character is retained by the choice of supercell shape, which is a  $2 \times 2 \times 2$  configuration of the ground state and further simplifies the calculation and comparison of structural and electronic properties among structures of varying degree of order.

Figure 5 shows the elastic constants ( $C$ ) calculated for various structures of  $\text{ZnGeN}_2$  with LRO parameters ranging from 0 to 1. Highly disordered structures have a greater variability in all  $C$  than more ordered structures but a linear change in  $C$  can be identified with  $S$  in some instances. For example, the strongest trends are in  $C_{22}$  and  $C_{33}$ , which increase with slopes of 19 and 16 GPa per change in order parameter.  $C_{11}$ ,  $C_{44}$ ,  $C_{55}$ , and  $C_{66}$  all have slopes between 4 and 8 GPa.  $C_{12}$  and  $C_{13}$  have weaker slopes, below 2 GPa, and  $C_{23}$  has the opposite trend, with a 3-GPa decrease with  $S$ . These changes of nearly 10% are small compared to the percent change in some of the electronic properties. The effects of the lower values of  $C_{22}$  and  $C_{33}$  for disordered  $\text{ZnGeN}_2$  are partially canceled by the increased interface strain with GaN as the lattice parameter increases for the disordered material. As can be seen from the values in Fig. 5 from Ref. [20], the change in elastic moduli with the long-range order is less than the disagreement in calculated elastic moduli in the literature for ordered  $\text{ZnGeN}_2$ .

The percent change in dielectric constants with the LRO parameter is larger than those of the elastic moduli, with

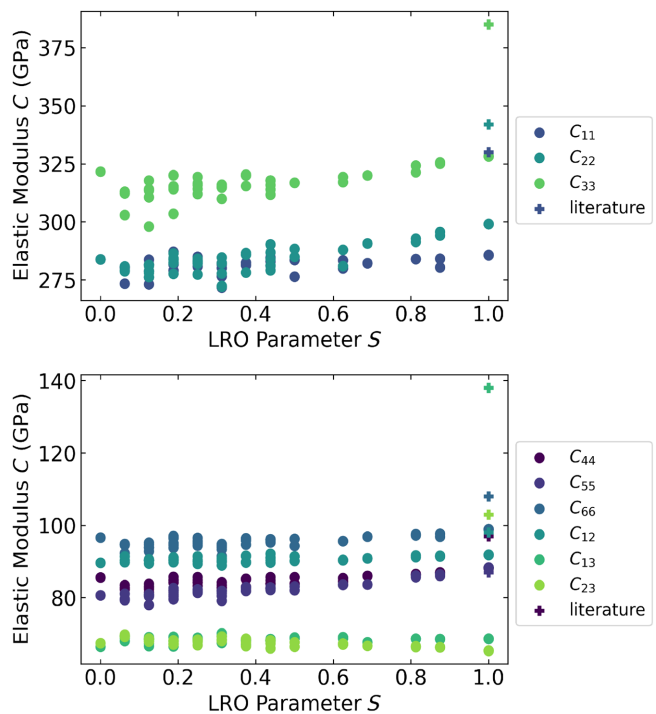


FIG. 5. The elastic moduli of  $\text{ZnGeN}_2$  as a function of the long-range cation order. The literature values are taken from Ref. [20].

average decreases of 21%, 13%, and 16% for  $\varepsilon_{11}$ ,  $\varepsilon_{22}$  and  $\varepsilon_{33}$ , respectively, as plotted in Fig. 6. In all three directions, the change gives higher dielectric constants in more disordered material, reflecting the general correlation between  $\varepsilon$  and the magnitude of the band-gap energy [43]. The calculations of dielectric constants predictably yield higher variability in mostly disordered material as well, because the dielectric properties are sensitive to the exact charge distribution in each supercell. Still, these changes play only a modest role in device design.

In Fig. 7, only piezoelectric coefficients that are nonzero for the ordered form of  $\text{ZnGeN}_2$  are listed. Due to the

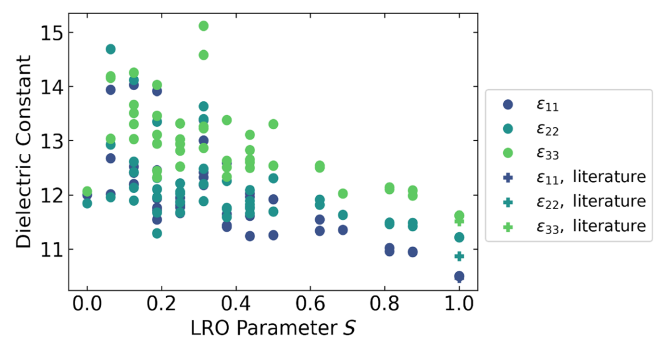


FIG. 6. The dielectric constants of  $\text{ZnGeN}_2$  as a function of the long-range cation order. The literature values are taken from Ref. [20].

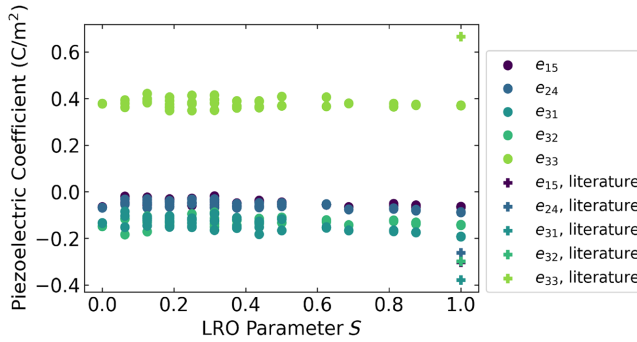


FIG. 7. The piezoelectric coefficients of ZnGeN<sub>2</sub> as a function of the long-range cation order. The literature values are taken from Ref. [20].

mechanism by which disorder is introduced in these structures through Monte Carlo simulations, the real symmetry of the structures is reduced and directional constants that are zero in an orthorhombic structure have nonzero values in some cases. For comparison, we focus on the five parameters represented in Fig. 7. Again, any changes in the property with order are fairly weak. Only  $e_{31}$  exhibits an appreciable change, increasing in magnitude by roughly 40% between full disorder and LRO. Each of the values becomes more negative with increased order, leading to a small decrease in magnitude for  $e_{33}$  and slight increases in magnitude for  $e_{15}$ ,  $e_{24}$ , and  $e_{32}$ .

Piezoelectric and spontaneous polarization sum together at an interface dictating the bound charge associated with a given surface. However, in order to calculate the spontaneous polarization of a structure, a nonpolar reference is needed [44,45]. In the case of disordered structures, no such convenient reference exists, but if the disordered structure forms an insulating interface with another material, the difference in formal polarization across that interface can be determined from DFT per the interface theorem [46,47].

The disordered structures that we use in this study are too large to perform interface calculations with GaN, making it difficult to confirm the insulating character of the interface of these heterostructures. However, we can confirm that both the GaN substrate structure used and all disordered structures strained to GaN in (001) used here do exhibit a band gap, even in the DFT with Hubbard  $U$  parameter (DFT+ $U$ ) formalism, which underestimates band gaps [31,48]. Likewise, the straddling character of the disordered band offsets described previously suggests that the interface itself remains insulating, which would not hold true if the offset were of the broken type-III variety. Different structures are used for the band offset and for polarization calculations due to the trade-offs between capturing disorder for accurate density of states and the limitations on supercell size imposed by the more computationally expensive polarization calculations. However,

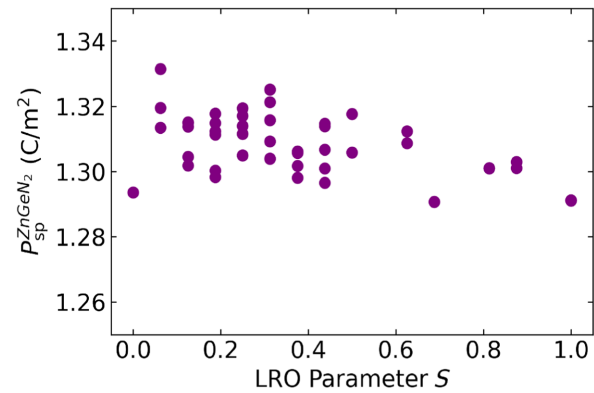


FIG. 8. The spontaneous-polarization constant of ZnGeN<sub>2</sub> in [001] as a function of the long-range cation order.

structures are chosen to maintain a realistic ordering character between supercell sizes. Using the assumption of an insulating interface, we then calculate the difference in polarization between disordered ZnGeN<sub>2</sub> and GaN.

Figure 8 shows the spontaneous polarization of ZnGeN<sub>2</sub> calculated from Born effective charges. For the purposes of epitaxial growth aligning the [001] direction in ZnGeN<sub>2</sub> to that of GaN, only the corresponding direction of  $P_{sp}$  is of interest. The spontaneous-polarization values are slightly larger for more disordered structures than for more ordered structures; however, the values prove highly variable at any given order parameter. The data set of structures represented in this figure are generated through Monte Carlo simulations from 46 seed structures, each containing 128 atoms, allowing for multiple configurations with similar or identical order parameters [24]. The method of comparing polarization between structures through the Born effective charge to arrive at an effective spontaneous polarization avoids the multivalued nature of the formal polarization, which requires the determination of the branch of polarization [34].

The bound charge at an interface is determined by summing the difference in spontaneous polarization between the component materials and the relevant piezoelectric terms multiplied by their respective strains.

The following equation—adapted from Ref. [34] and based on the interface theorem of Ref. [46], established for a polarization value comparable between theory and experiment outlined in Ref. [44]—defines the bound charge  $\sigma_b$  for the interface between a wurtzite and an orthorhombic material, in this case GaN and ordered ZnGeN<sub>2</sub>:

$$\sigma_b = [P_{sp}^{GaN} + e_{31}^{GaN}(\epsilon_1^{GaN} + \epsilon_2^{GaN}) + e_{33}^{GaN}\epsilon_3^{GaN}] - [P_{sp}^{ZnGeN_2} + e_{31}^{ZnGeN_2}\epsilon_1^{ZnGeN_2} + e_{32}^{ZnGeN_2}\epsilon_2^{ZnGeN_2} + e_{33}^{ZnGeN_2}\epsilon_3^{ZnGeN_2}], \quad (1)$$

where  $P_{sp}$  is the spontaneous polarization of a given material, the  $e_{ij}$  are the piezoelectric coefficients, and the  $\epsilon_i$

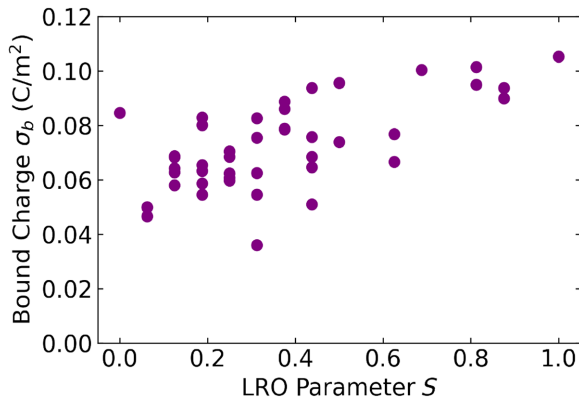


FIG. 9. The bound charge at the interface of ZnGeN<sub>2</sub> and GaN.

are the strain components for each given direction. For the wurtzite structure of GaN, which we relax to be the substrate,  $\epsilon_1^{\text{GaN}} = \epsilon_2^{\text{GaN}} = \epsilon_3^{\text{GaN}} = 0$ . Replacing the two spontaneous-polarization constants with their difference  $\Delta P_{\text{sp}}^{\text{interface}}$  then yields

$$\sigma_b = \Delta P_{\text{sp}}^{\text{interface}} - e_{31}^{\text{ZnGeN}_2} \epsilon_1^{\text{ZnGeN}_2} - e_{32}^{\text{ZnGeN}_2} \epsilon_2^{\text{ZnGeN}_2} - e_{33}^{\text{ZnGeN}_2} \epsilon_3^{\text{ZnGeN}_2}. \quad (2)$$

These calculated bound charges for ZnGeN<sub>2</sub>-GaN interfaces are shown in Fig. 9. While the bound charge comprises a spontaneous and a piezoelectric contribution, the quantity itself does not reveal if one of these terms dominates. Because the spontaneous polarization is slightly greater for the disordered structures, the difference in polarization between ZnGeN<sub>2</sub> and GaN also grows with disorder. Meanwhile, the piezoelectric term shrinks with disorder as the ZnGeN<sub>2</sub> becomes more “wurtzitelike” and the lateral lattice parameters become more similar to those of GaN. The combination of these trends results in piezoelectric contributions roughly double that of the spontaneous term for mostly ordered structures, which shrink with increasing disorder to roughly the same magnitude as each other in the disordered limit. The use of GaN as the substrate material provides a negative spontaneous term and a net positive sum of piezoelectric terms for all order parameters. The relationship between these terms yields a slight increasing trend in bound charge with order parameter, with a variability similar to that seen for spontaneous polarization in Fig. 8.

#### IV. OUTLOOK FOR DEVICES

Until this point, we have examined bulk properties and the interface of ZnGeN<sub>2</sub> with GaN as they change with site ordering, but how do these properties and the interface

construction influence emission processes in a device? Fig. 4 confirms previous predictions that increasing disorder lowers the energy gap between occupied and unoccupied states of ZnGeN<sub>2</sub> into the region of green emission at around  $S = 0.97$  and lower energies for lower degrees of order. Beyond this assessment, the sudden increase in the VBM when disorder is introduced to the otherwise pristine structure shifts the band offset with GaN from being type II to type I. Our previous study has examined how introducing disorder to reduce band gaps also creates localized states and the energy loss associated with the Stokes shift upon electron-hole recombination causes energy to be nonradiatively emitted as heat on the order of 0.6 eV per electron-hole pair [13]. This study shows that Zn<sub>Ge</sub> + Ge<sub>Zn</sub> pairs can be used to reach the green and amber emission desired for color-mixed LEDs but the disorder may come at the cost of nonradiative losses, which lower device efficiencies from their theoretical maximum internal quantum efficiency. Advances in material quality coupled with a qualitative method for linking measured optical properties with order parameter are needed to determine the effects of localized defect states and to assess the feasibility of controlling site ordering.

Having established that disordered ZnGeN<sub>2</sub> fits the minimum criteria for utility as part of a green-emitting quantum well, we can address some of the challenges facing the more extensively studied InGaN-GaN system for its application in closing the “green gap.” InGaN—particularly in the composition range of 10–15% In content—is the basis of the majority of inorganic solid-state lighting technology today, so we use this composition as a baseline to determine acceptable strain and polarization limitations in ZnGeN<sub>2</sub>. Namely, InGaN suffers from (1) point-defect incorporation in low-temperature growths, (2) immiscibility driving phase separation, (3) lattice mismatch with GaN, which causes extended dislocations to form and leads to large piezoelectric fields, and (4) poor wave-function overlap between electrons and holes due to polarization effects [49]. The last three items on this list increase in severity with the higher In content needed to reach green emission [50]. These issues are not exhaustive for either InGaN or ZnGeN<sub>2</sub>; however, we can immediately negate some of these questions for ZnGeN<sub>2</sub>. For instance, the first issue of detrimental point defects is not applicable in parallel to ZnGeN<sub>2</sub> as antisites underlie the premise of site disorder and while they do create localization, which warrants further study and experimentation, their incorporation is key for targeting the emission properties desired. Defect studies have highlighted native antisites as the most thermodynamically favorable point defect in the system, justifying the use of these native defects for controlling ordering [15,18,51]. Likewise, the miscibility gap of InGaN, which largely prevents solid solution for intermediate In content  $0.2 < \text{In}/(\text{Ga} + \text{In}) < 0.8$  is not present in ZnGeN<sub>2</sub> [15,52,53].

The effects of disorder on properties allow us to comment on the magnitude of changes of other device characteristics that depend on interface interactions as well as bulk properties. In the present study, we show that cation disorder leads to varied elastic moduli that largely shrink relative to the ordered structure by around 10%. The stiffness of the lattice in lateral directions determines the likelihood of threading dislocations along with the magnitude and direction of strain in the system. The stiffer the material, the less compliant and more likely the system is to form threading dislocations and other extended defects to accommodate high strain. These extended defects are common in InGaN/GaN heterostructures with an In content greater than  $\text{In}/(\text{Ga} + \text{In}) = 0.05$  [54–56] because the increased lattice mismatch with higher In content in InGaN places significant strain on the lattice even though InN is much more compliant than GaN, with  $C_{33}$  of 398 GPa and 224 GPa for GaN and InN, respectively [35]. The lower elastic moduli of disordered ZnGeN<sub>2</sub> than ordered ZnGeN<sub>2</sub> are comparable to those of In<sub>0.1</sub>Ga<sub>0.9</sub>N; however, the similar lattice constant of both ordered and disordered ZnGeN<sub>2</sub> to GaN provides less strain and therefore a lower likelihood of threading dislocations inherent to the heterostructure.

Besides extended defect behavior, the elastic moduli also determine the CBM and VBM positions of strained materials. In growth direction [001], the relationship between the band-edge energies is derived from the expressions for band-edge splitting from  $\mathbf{k} \cdot \mathbf{p}$  theory [57,58] and the Luttinger-Kohn model [59], where the following equations give the dependence of the valence subbands [60,61]:

$$\begin{aligned} E_{\text{HH}} &= -E_i - P_\epsilon - Q_\epsilon, \\ E_{\text{LH}} &= -E_i - P_\epsilon + \frac{1}{2}(Q_\epsilon - \Delta + \sqrt{(Q_\epsilon + \Delta)^2 + 8Q_\epsilon^2}), \\ E_{\text{SH}} &= -E_i - P_\epsilon + \frac{1}{2}(Q_\epsilon - \Delta - \sqrt{(Q_\epsilon + \Delta)^2 + 8Q_\epsilon^2}), \end{aligned} \quad (3)$$

where

$$\begin{aligned} P_\epsilon &= -a_v \epsilon_{11} (1 - C_{12}/C_{11}) - a_v \epsilon_{22} (1 - C_{12}/C_{22}), \\ Q_\epsilon &= -\frac{1}{2} b_v \epsilon_{11} (1 + 2C_{12}/C_{11}) - \frac{1}{2} b_v \epsilon_{22} (1 + 2C_{12}/C_{22}), \end{aligned} \quad (4)$$

and  $E_{\text{HH}}$ ,  $E_{\text{LH}}$ , and  $E_{\text{SH}}$  are the energies of the heavy, light, and split-off holes, respectively.  $E_i$  is the ionization energy and  $\Delta$  is the spin-orbital splitting energy.  $a_v$  and  $b_v$  are both valence-band deformation potentials [62,63] and correspond to the directions of strain  $\epsilon_{ij}$  and elastic moduli  $C_{ij}$  [64]. The elastic moduli or, more specifically, the ratios  $C_{12}/C_{11}$  and  $C_{12}/C_{22}$ , have a partial self-cancelling relationship with themselves between factors  $P_\epsilon$  and  $Q_\epsilon$

depending on the deformation potentials  $a_v$  and  $b_v$ . Using the elastic moduli from Fig. 5,  $C_{12}/C_{11}$  is not significantly affected by ordering; however,  $C_{12}/C_{22}$  increases by 5% from the ordered structure to a fully disordered structure. This change in ratio of the elastic moduli raises  $E_{\text{HH}}$  modestly and lowers  $E_{\text{LH}}$  and  $E_{\text{SH}}$  with a decreased degree of order.

Additionally assuming the [001] growth direction,  $C_{12}/C_{11}$  and  $C_{12}/C_{22}$  contribute to band splitting in the conduction band at the  $X$  and  $R$  band points when the material is strained. Equation (5) gives the dependence of the conduction subbands on the elastic moduli [60,61]:

$$\begin{aligned} E_{[100]}^X &= 2\Xi_d^X \epsilon_{11} (1 - C_{12}/C_{11}) + \Xi_u^X \epsilon_{11}, \\ E_{[010]}^X &= 2\Xi_d^X \epsilon_{22} (1 - C_{12}/C_{22}) + \Xi_u^X \epsilon_{22}, \\ E_{[001]}^X &= \Xi_d^X \epsilon_{11} (1 - C_{12}/C_{11}) + \Xi_d^X \epsilon_{22} (1 - C_{12}/C_{22}), \\ &\quad - \Xi_u^X \epsilon_{11} (C_{12}/C_{11}) - \Xi_u^X \epsilon_{22} (C_{12}/C_{22}), \\ E_{<111>}^R &= \Xi_d^R \epsilon_{11} (1 - C_{12}/C_{11}) + \Xi_d^R \epsilon_{22} (1 - C_{12}/C_{22}), \\ &\quad + \frac{1}{3} \Xi_u^R \epsilon_{11} (1 - C_{12}/C_{11}) \\ &\quad + \frac{1}{3} \Xi_u^R \epsilon_{22} (1 - C_{12}/C_{22}), \end{aligned} \quad (5)$$

where  $E_{[ijk]}^X$  and  $E_{ijk}^R$  are the conduction-subband energies at  $X$  and  $R$ , respectively, in direction  $[ijk]$  or the family of directions  $<ijk>$ .  $\Xi_d^{X,R}$  and  $\Xi_u^{X,R}$  are the respective conduction-band deformation potentials at  $X$  and  $R$ . Comparing  $C_{11}$  and  $C_{22}$ , which align more closely in disordered material, this model predicts more isotropy or similarity in electronic bands at  $X$  in disordered material. With the consideration that the change in  $C_{12}/C_{22}$  with the LRO parameter is more significant than that in  $C_{12}/C_{11}$ , we can also expect a large decrease in the conduction band at  $R$  in disordered ZnGeN<sub>2</sub>.

Besides elastic contributions to the band structure, polarization also plays a strong role in the band shapes in a device. The similar values of the spontaneous polarization in GaN and ZnGeN<sub>2</sub> lead to small differences in polarization, so the overall bound charge remains small. The reduction of strain further shrinks this quantity in disordered structures. The predicted bound charge at this interface is similar in magnitude to that calculated for In<sub>0.2</sub>Ga<sub>0.8</sub>N/GaN and Al<sub>0.2</sub>Ga<sub>0.8</sub>N/GaN [34] and measured for Al<sub>0.25</sub>Ga<sub>0.75</sub>N/GaN [65], where bound-charge estimates range from 0.03 C/m<sup>2</sup> to 0.10 C/m<sup>2</sup>. The values of bound charge indicate a modest slope of these bands in an LED; however, within the precision of Fig. 9, this quantity is not strongly affected by cation order in ZnGeN<sub>2</sub> and similar polarization effects from ZnGeN<sub>2</sub> should be expected as for In<sub>x</sub>Ga<sub>1-x</sub>N, where  $0 < x < 0.1$ .

Where the elastic moduli and polarization do not exhibit high sensitivity to ordering, the band engineering is

nonetheless greatly affected by the change in offsets with ordering, which is predicted to play the largest role in device design of the calculated properties. Our calculations of band offsets in the ordered interface indicate a small staggered offset, which quickly becomes a straddling offset for appreciable site disorder in ZnGeN<sub>2</sub>. In the case of staggered offsets, polarization and a strong electric field are desirable for guiding the recombination of electrons and holes at the points of quantum wells in energy and space. In contrast, in the case of straddling offsets, these points of the quantum wells do not align vertically in space, so a negligible net internal electric field is desired in order to make use of recombination along the entirety of each quantum well.

Another variable for tuning the emission in ZnGeN<sub>2</sub> active layers is the alloying of Sn along with Ge on the group-IV site. Alloying with ZnSnN<sub>2</sub> introduces similar strain to InN alloyed with GaN but avoids the miscibility gap of InGaN and similarly reduces the band gap of the active layer as a function of the composition [53,66]. Ordering in ZnSnN<sub>2</sub> also plays a comparable role in CBM lowering and VBM raising [67], although it remains to be studied how cation disorder manifests in Zn(Sn, Ge)N<sub>2</sub>: either mostly on the group-IV site or evenly throughout the cation sublattice.

## V. CONCLUSIONS

We present a computational model for the effects of cation disorder in ZnGeN<sub>2</sub> on the interface properties with GaN and the resulting implications for device design. These calculations of the polar interface of ZnGeN<sub>2</sub> and GaN use a hybrid functional to investigate the wurtzite-derived system most comparable to the material and the growth direction sought for LED synthesis. The band offsets of the heterostructure change from a staggered offset when we employ ordered material to straddling upon the narrowing of the ZnGeN<sub>2</sub> band gap with increased disorder. Small fractions of antisite defects in ZnGeN<sub>2</sub> lead to raised valence bands that separate from the band continuum. These defect states persist as the valence-band continuum rises and the conduction-band continuum sinks with a decreasing LRO parameter. The elastic moduli show weak trends with disorder, as do the relevant tensor quantities of the dielectric constant and the piezoelectric coefficient. The bound charge at the ZnGeN<sub>2</sub>-GaN interface remains comparable in magnitude to that measured in binary- and ternary-nitride heterostructures for all LRO parameters and even decreases with disorder.

The magnitudes of these changes in the structural and electronic properties provide a predictive template for band engineering in a ZnGeN<sub>2</sub>/GaN device. The band offsets are small in magnitude for the ordered structure and increase in magnitude for straddling offsets created with disordered ZnGeN<sub>2</sub>. These offset predictions, which are either small

type II or type I, indicate the need for additional potential barrier layers incorporated into a device to promote radiative recombination. The largest predicted challenges for incorporating disordered ZnGeN<sub>2</sub> for achieving efficient green emission are targeting specific band-offset values and mitigating localized states generated from native antisites.

## VI. METHODS

### A. Monte Carlo

The cation disorder is simulated in ZnGeN<sub>2</sub> by swapping cations in the system using Monte Carlo simulation. We used the Clusters Approach to Statistical Mechanics (CASM) software as a framework for setting up simulations. The details on training our cluster expansion and performing simulations are fully described in Ref. [24]. We use 128-atom  $2 \times 2 \times 2$  supercells of the 16-atom ZnGeN<sub>2</sub> primitive cell for the structures used in the device-parameter calculations. For the bulk and interface structures generated as a part of this study, see the Supplemental Material [68].

### B. First-principles calculations

#### 1. Bulk relaxation

All bulk structures in this work are first relaxed in volume, shape, and ionic positions using DFT+U. We use the PBE-type GGA [69] for the relaxations. For cells with more than 100 atoms, we use the gamma-point-only version of VASP with a single gamma-centered  $k$  point. For smaller 16-atom ordered cells, we use a  $6 \times 6 \times 6$   $k$ -point grid and the standard version of VASP. The energy and force convergence criteria for ionic relaxation are set to  $10^{-5}$  eV and  $0.02$  eV Å<sup>-1</sup>, respectively, on each atom. A Coulomb potential of  $U - J = 6$  eV is applied to the Zn  $d$  orbital according to the Dudarev approach [70]. Kresse-Joubert projector augmented-wave data sets are used with pseudopotentials from VASP version 4.6 (Ge\_d, N\_s, and Zn) and an energy cutoff of 380 eV [71].

#### 2. Interfaces

The band offsets between GaN and ordered ZnGeN<sub>2</sub> are determined through a process of constructing an interface and aligning the potentials of the materials. The bulk materials are first relaxed using DFT+U, employing the parameters described in the previous subsection. Separate calculations are used to examine the strain of each film material to its respective substrate [ZnGeN<sub>2</sub> to GaN and GaN to ZnGeN<sub>2</sub> in Figs. 2(a) and 2(b), respectively], where the  $a$  and  $b$  lattice parameters are replaced by those of the substrate and atoms are only allowed to relax in [001]. A periodic arrangement of strained and relaxed cells contains alternating stacks of  $1 \times 1 \times 8$  supercells of each film and substrate. The atomic layers of the two materials

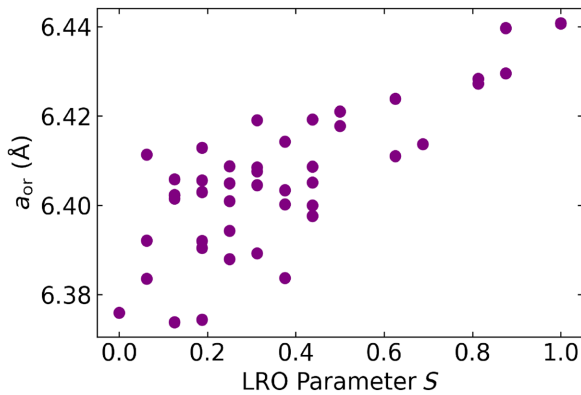


FIG. 10. Orthorhombic lattice parameter  $a$  of the 128-atom  $\text{ZnGeN}_2$  configurations scaled to the conventional cell size.

are centered and stacked using the atomic simulation environment (ASE) software package [72]. No vacuum layer is used in the superstructure, effectively creating a set of infinitely periodic quantum wells. The superstructure created by stacking  $\text{ZnGeN}_2$  on GaN is then further relaxed using DFT+ $U$ , again only allowing atomic movement in [001] to find the proper spacing at the two interfaces created.

To obtain a band alignment, the electrostatic potential is taken from the  $\text{ZnGeN}_2/\text{GaN}$  superstructure relaxation in order to determine the potential step at the interface between the two materials. The characteristics of this step in potential are then taken by integrating the potential twice within each layer and taking a linear regression to find the slope of the potential for both GaN and  $\text{ZnGeN}_2$  as well as their intercepts with the energy axis. The VBM and CBM of GaN and  $\text{ZnGeN}_2$  are taken from the respective relaxed and strained bulk calculations and these values are added to the step in potential.

For disordered cells, which are too large to relax as part of an interface, the ordered potential offsets are used along

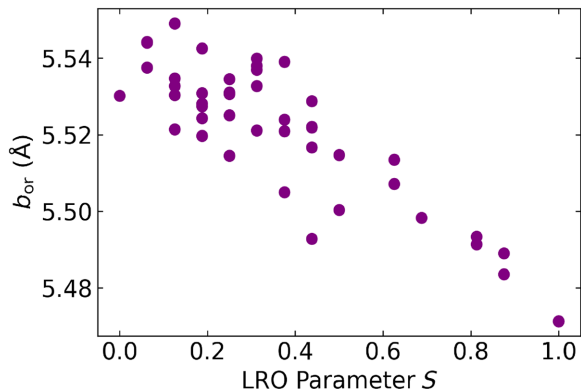


FIG. 11. Orthorhombic lattice parameter  $b$  of the 128-atom  $\text{ZnGeN}_2$  configurations scaled to the conventional cell size.

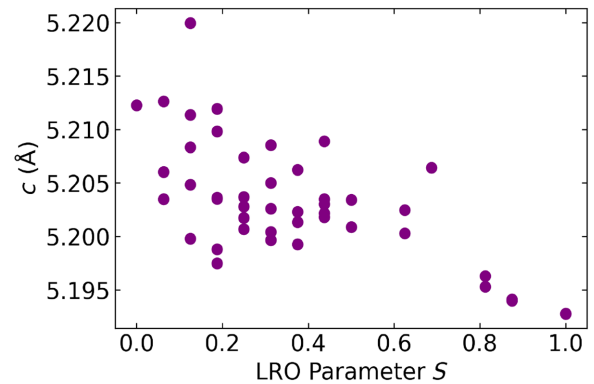


FIG. 12. Lattice parameter  $c$  of the 128-atom  $\text{ZnGeN}_2$  configurations scaled to the conventional cell size (same for wurtzite or orthorhombic cell).

with band energies calculated in the single-shot hybrid (SSH+V) for strained  $\text{ZnGeN}_2$  in different ion configurations [67,73]. The single-shot functional uses fixed wave functions from the initial DFT+ $U$  calculation. The mixing parameter  $\alpha = 0.19$  without range separation and the Coulomb potential  $V_{\text{Zn-d}} = -1.5$  eV are fitted to reproduce the band energies and density of states of a  $GW$  calculation [74]. The band offsets for disordered  $\text{ZnGeN}_2$  structures contain an additional potential alignment based on this change in volume [13].

To determine the band lineup for InGaN alloys in Fig. 4, we estimate the change of the InGaN band edges relative to GaN in the following way. First, the  $GW$  band positions for GaN and InN, available in the NRELMatDB [31,32], are linearly interpolated (i.e., neglecting bowing effects). Second, using an InGaN-alloy supercell calculation on the DFT level, we determine the potential alignment due to the composition and volume change in InGaN relative to GaN, in a similar fashion as in the case of disordered  $\text{ZnGeN}_2$  [13]. Adding both contributions to the average potential on the GaN side of the interface yields an approximate result for the  $\text{ZnGeN}_2/\text{InGaN}$  offsets. Additional substrate or film strain effects due to InGaN alloying are not considered.

### 3. Material properties

The elastic moduli, piezoelectric coefficients, and dielectric constants are determined with more stringent relaxation criteria than other calculations by using energy- and force-convergence criteria of  $10^{-9}$  eV and  $0.001$  eV  $\text{\AA}^{-1}$ , respectively. The elastic moduli and the polarization are calculated using the finite-differences approach [75], while the calculations of the piezoelectric coefficient use perturbation theory [76]. The polarization is calculated from the Born effective charge, lattice parameters, and displacements of cation layers [34,45].

## ACKNOWLEDGMENTS

This work was supported by the U.S. Department of Energy (DOE), Office of Energy Efficiency and Renewable Energy, Buildings Technologies Office. The National Renewable Energy Laboratory is operated for the DOE by the Alliance for Sustainable Energy, LLC, under Contract No. DE-AC36-08GO28308. This work used high-performance computing resources located at the NREL and sponsored by the Office of Energy Efficiency and Renewable Energy. The views expressed in the paper do not necessarily represent the views of the DOE or the U.S. government. The U.S. government retains and the publisher, by accepting the article for publication, acknowledges that the U.S. government retains a nonexclusive, paid-up, irrevocable, worldwide license to publish or reproduce the published form of this work, or allow others to do so, for government purposes. J.C. and M.M. undertook the investigation. J.C., M.B.T., and S.L. were responsible for the conceptualization of the study. J.C. and M.M. oversaw the methodology and the formal analysis. J.C. was responsible for visualization and for the software and the writing of the paper. M.B.T. and A.T. handled the funding acquisition. All of the authors took part in marshalling the resources and editing the text. G.T., A.T., and S.L. supervised the project.

The data that support the findings of this study are available from the corresponding author upon reasonable request.

## APPENDIX: LATTICE PARAMETERS OF SIMULATED STRUCTURES

The lattice parameters of structures used in Sec. III B are shown in Figs. 10–12. Figures 10, 11, and 12 provide  $a$ ,  $b$ , and  $c$ , respectively, for the orthorhombic configuration of ZnGeN<sub>2</sub> as they change depending on LRO. The decrease in  $a$  and increase in  $b$ , where  $a > b$  as the material tends toward disorder indicates a shift away from the orthorhombic structure toward the wurtzitelike structure.

- 
- [1] W. Sun, C. J. Bartel, E. Arca, S. R. Bauers, B. Matthews, B. Orvañanos, B.-R. Chen, M. F. Toney, L. T. Schelhas, W. Tumas, *et al.*, A map of the inorganic ternary metal nitrides, *Nat. Mater.* **18**, 732 (2019).
  - [2] R. R. Schnepf, J. J. Cordell, M. B. Tellekamp, C. L. Melamed, A. L. Greenaway, A. Mis, G. L. Brennecka, S. Christensen, G. J. Tucker, E. S. Toberer, *et al.*, Utilizing site disorder in the development of new energy-relevant semiconductors, *ACS Energy Lett.* **5**, 2027 (2020).
  - [3] Y. Hinuma, T. Hatakeyama, Y. Kumagai, L. A. Burton, H. Sato, Y. Muraba, S. Iimura, H. Hiramatsu, I. Tanaka, H. Hosono, *et al.*, Discovery of earth-abundant nitride semiconductors by computational screening and high-pressure synthesis, *Nat. Commun.* **7**, 1 (2016).
  - [4] T. M. Christian, D. A. Beaton, K. Mukherjee, K. Alberi, E. A. Fitzgerald, and A. Mascarenhas, Amber-green light-emitting diodes using order-disorder Al<sub>x</sub>In<sub>1-x</sub>P heterostructures, *J. Appl. Phys.* **114**, 074505 (2013).
  - [5] E. Arca, J. D. Perkins, S. Lany, A. Mis, B.-R. Chen, P. Dippo, J. L. Partridge, W. Sun, A. Holder, A. C. Tamboli, *et al.*, Zn<sub>2</sub>SbN<sub>3</sub>: Growth and characterization of a metastable photoactive semiconductor, *Mater. Horiz.* **6**, 1669 (2019).
  - [6] A. L. Greenaway, A. L. Loutris, K. N. Heinselman, C. L. Melamed, R. R. Schnepf, M. B. Tellekamp, R. Woods-Robinson, R. Sherbondy, D. Bardgett, S. Bauers, *et al.*, Combinatorial synthesis of magnesium tin nitride semiconductors, *J. Am. Chem. Soc.* **142**, 8421 (2020).
  - [7] A. Mis, S. Lany, G. L. Brennecka, and A. Tamboli, Exploring the phase space of Zn<sub>2</sub>SbN<sub>3</sub>, a novel semiconducting nitride, *J. Mater. Chem. C* **9**, 13904 (2021).
  - [8] C. G. Van de Walle, Optoelectronic devices based on ZnGeN<sub>2</sub> integrated with group III-V nitrides, September 19, 2000. U.S. Patent 6,121,639.
  - [9] L. D. Zhu, P. H. Maruska, P. E. Norris, P. W. Yip, and L. O. Bouthillette, Epitaxial growth and structural characterization of single crystalline ZnGeN<sub>2</sub>, *Mater. Res. Soc. Int. J. Nitride Semicond. Res.* **4**, 149 (1999).
  - [10] L. Han, K. Kash, and H. Zhao, in *Light-Emitting Diodes: Materials, Devices, and Applications for Solid State Lighting XVIII*, volume 9003, p. 90030W. International Society for Optics and Photonics, 2014.
  - [11] D. Skachkov, P. C. Quayle, K. Kash, and W. R. L. Lambrecht, Disorder effects on the band structure of ZnGeN<sub>2</sub>: Role of exchange defects, *Phys. Rev. B* **94**, 205201 (2016).
  - [12] M. S. Haseman, Md. R. Karim, D. Ramdin, B. A. Noesges, E. Feinberg, B. H. D. Jayatunga, W. R. L. Lambrecht, M. Zhu, J. Hwang, K. Kash, H. Zhao, and L. J. Brillson, Deep level defects and cation sublattice disorder in ZnGeN<sub>2</sub>, *J. Appl. Phys.* **127**, 135703 (2020).
  - [13] J. J. Cordell, G. J. Tucker, A. Tamboli, and S. Lany, Bandgap analysis and carrier localization in cation-disordered ZnGeN<sub>2</sub>, *APL Mater.* **10**, 011112 (2022).
  - [14] E. W. Blanton, K. He, J. Shan, and K. Kash, Characterization and control of ZnGeN<sub>2</sub> cation lattice ordering, *J. Cryst. Growth* **461**, 38 (2017).
  - [15] C. L. Melamed, J. Pan, A. Mis, K. Heinselman, R. R. Schnepf, R. Woods-Robinson, J. Cordell, S. Lany, E. Toberer, and A. C. Tamboli, Combinatorial investigation of structural and optical properties of cation-disordered ZnGeN<sub>2</sub>, *J. Mater. Chem. C* **8**, 8736 (2020).
  - [16] A. Punya and W. R. L. Lambrecht, Band offsets between ZnGeN<sub>2</sub>, GaN, ZnO, and ZnSnN<sub>2</sub> and their potential impact for solar cells, *Phys. Rev. B* **88**, 75302 (2013).
  - [17] A. P. Jaroenjittichai, S. Lyu, and W. R. L. Lambrecht, Erratum: Band offsets between ZnGeN<sub>2</sub>, GaN, ZnO, and ZnSnN<sub>2</sub> and their potential impact for solar cells [phys. rev. b 88, 075302 (2013)], *Phys. Rev. B* **96**, 079907 (2017).
  - [18] S. Lyu, D. Skachkov, K. Kash, E. W. Blanton, and W. R. L. Lambrecht, Band Gaps, Band-Offsets, Disorder, Stability Region, and Point Defects in II-IV-N<sub>2</sub> Semiconductors, *Phys. Status Solidi (a)* **216**, 1800875 (2019).
  - [19] R. Cao, H.-X. Deng, J.-W. Luo, and S.-H. Wei, Origin of the anomalous trends in band alignment of GaX/ZnGeX<sub>2</sub>

- (X = N, P, As, Sb) heterojunctions, *J. Semicond.* **40**, 042102 (2019).
- [20] N. L. Adamski, D. Wickramaratne, and C. G. Van de Walle, Band alignments and polarization properties of the Zn-IV-nitrides, *J. Mater. Chem. C* **8**, 7890 (2020).
- [21] Md. R. Karim, B. A. Noesges, B. H. D. Jayatunga, M. Zhu, J. Hwang, W. R. L. Lambrecht, L. J. Brillson, K. Kash, and H. Zhao, Experimental determination of the valence band offsets of ZnGeN<sub>2</sub> and (ZnGe) 0.94 Ga0.12N<sub>2</sub> with GaN, *J. Phys. D: Appl. Phys.* **54**, 245102 (2021).
- [22] W. L. Bragg and E. J. Williams, The effect of thermal agitation on atomic arrangement in alloys, Proc. R. Soc. London Ser. A, Containing Papers Math. Phys. Charact. **145**, 699 (1934).
- [23] W. L. Bragg and E. J. Williams, The effect of thermal agitation on atomic arrangement in alloys—II, Proc. R. Soc. London Ser. A—Math. Phys. Sci. **151**, 540 (1935).
- [24] J. J. Cordell, J. Pan, A. C. Tamboli, G. J. Tucker, and S. Lany, Probing configurational disorder in ZnGeN<sub>2</sub> using cluster-based Monte Carlo, *Phys. Rev. Mater.* **5**, 024604 (2021).
- [25] M. B. Tellekamp, M. K. Miller, A. D. Rice, and A. C. Tamboli, Heteroepitaxial ZnGeN<sub>2</sub> on AlN: Growth, structure, and optical properties, *Cryst. Growth Des.* **22**, 1270 (2022).
- [26] Md. R. Karim, B. H. D. Jayatunga, Z. Feng, K. Kash, and H. Zhao, Metal-organic chemical vapor deposition growth of ZnGeN<sub>2</sub> films on sapphire, *Cryst. Growth Des.* **19**, 4661 (2019).
- [27] M. B. Tellekamp, C. L. Melamed, A. G. Norman, and A. Tamboli, Heteroepitaxial integration of ZnGeN<sub>2</sub> on GaN buffers using molecular beam epitaxy, *Cryst. Growth Des.* **20**, 1868 (2020).
- [28] T. Misaki, A. Wakahara, H. Okada, and A. Yoshida, Epitaxial growth and characterization of ZnGeN<sub>2</sub> by metalorganic vapor phase epitaxy, *J. Cryst. Growth* **260**, 125 (2004).
- [29] C. L. Melamed, M. B. Tellekamp, J. S. Mangum, J. D. Perkins, P. Dippo, E. S. Toberer, and A. C. Tamboli, Blue-green emission from epitaxial yet cation-disordered ZnGeN<sub>2-x</sub>O<sub>x</sub>, *Phys. Rev. Mater.* **3**, 051602 (2019).
- [30] C. Stender and K. Alberi, Al<sub>x</sub>In<sub>1-x</sub>P LEDs with II-VI cladding layers for efficient red and amber emission. final scientific & technical report. Technical report, MicroLink Devices Inc., Niles, Illinois, 2017.
- [31] S. Lany, Band-structure calculations for the 3d transition metal oxides in *GW*, *Phys. Rev. B* **87**, 085112 (2013).
- [32] S. Lany, Semiconducting transition metal oxides, *J. Phys.: Condens. Matter* **27**, 283203 (2015).
- [33] I. Petousis, D. Mrdjénovich, E. Ballouz, M. Liu, D. Winston, W. Chen, T. Graf, T. D. Schladt, K. A. Persson, and F. B. Prinz, High-throughput screening of inorganic compounds for the discovery of novel dielectric and optical materials, *Sci. Data* **4**, 1 (2017).
- [34] C. E. Dreyer, A. Janotti, C. G. Van de Walle, and D. Vanderbilt, Correct Implementation of Polarization Constants in Wurtzite Materials and Impact on III-Nitrides, *Phys. Rev. X* **6**, 021038 (2016).
- [35] I. Vurgaftman, J. R. Meyer, and L. R. Ram-Mohan, Band parameters for III-V compound semiconductors and their alloys, *J. Appl. Phys.* **89**, 5815 (2001).
- [36] A. Jain, S. P. Ong, G. Hautier, W. Chen, W. D. Richards, S. Dacek, S. Cholia, D. Gunter, D. Skinner, G. Ceder, *et al.*, Commentary: The materials project: A materials genome approach to accelerating materials innovation, *APL Mater.* **1**, 011002 (2013).
- [37] A. F. Wright, Elastic properties of zinc-blende and wurtzite AlN, GaB, and InN, *J. Appl. Phys.* **82**, 2833 (1997).
- [38] M. De Jong, W. Chen, T. Angsten, A. Jain, R. Notestine, A. Gamst, M. Sluiter, C. K. Ande, S. Van Der Zwaag, J. J. Plata, *et al.*, Charting the complete elastic properties of inorganic crystalline compounds, *Sci. Data* **2**, 1 (2015).
- [39] T. R. Paudel and W. R. L. Lambrecht, First-principles calculations of elasticity, polarization-related properties, and nonlinear optical coefficients in Zn-IV-N<sub>2</sub> compounds, *Phys. Rev. B* **79**, 245205 (2009).
- [40] C. M. Lueng, H. L. W. Chan, C. Surya, and C. L. Choy, Piezoelectric coefficient of aluminum nitride and gallium nitride, *J. Appl. Phys.* **88**, 5360 (2000).
- [41] G. Kresse and J. Furthmüller, Efficient iterative schemes for *ab initio* total-energy calculations using a plane-wave basis set, *Phys. Rev. B* **54**, 11169 (1996).
- [42] J. Heyd, J. E. Peralta, G. E. Scuseria, and R. L. Martin, Energy band gaps and lattice parameters evaluated with the Heyd-Scuseria-Ernzerhof screened hybrid functional, *J. Chem. Phys.* **123**, 174101 (2005).
- [43] R. Ravichandran, A. X. Wang, and J. F. Wager, Solid state dielectric screening versus band gap trends and implications, *Opt. Mater.* **60**, 181 (2016).
- [44] R. D. King-Smith and D. Vanderbilt, Theory of polarization of crystalline solids, *Phys. Rev. B* **47**, 1651 (1993).
- [45] N. A. Spaldin, A beginner’s guide to the modern theory of polarization, *J. Solid State Chem.* **195**, 2 (2012).
- [46] D. Vanderbilt and R. D. King-Smith, Electric polarization as a bulk quantity and its relation to surface charge, *Phys. Rev. B* **48**, 4442 (1993).
- [47] R. Resta and D. Vanderbilt, in *Physics of Ferroelectrics*, p. 31. Springer, (2007).
- [48] I. Choudhuri and D. G. Truhlar, Hle17: An efficient way to predict band gaps of complex materials, *J. Phys. Chem. C* **123**, 17416 (2019).
- [49] J. Gruber, X. W. Zhou, R. E. Jones, S. R. Lee, and G. J. Tucker, Molecular dynamics studies of defect formation during heteroepitaxial growth of InGaN alloys on (0001) GaN surfaces, *J. Appl. Phys.* **121**, 195301 (2017).
- [50] J. Wu, When group-III nitrides go infrared: New properties and perspectives, *J. Appl. Phys.* **106**, 5 (2009).
- [51] D. Skachkov, A. P. Jaroenjittichai, L.-y. Huang, and W. R. L. Lambrecht, Native point defects and doping in ZnGeN<sub>2</sub>, *Phys. Rev. B* **93**, 155202 (2016).
- [52] D. Doppalapudi, S. N. Basu, K. F. Ludwig Jr, and T. D. Moustakas, Phase separation and ordering in InGaN alloys grown by molecular beam epitaxy, *J. Appl. Phys.* **84**, 1389 (1998).
- [53] P. Narang, S. Chen, N. C. Coronel, S. Gul, J. Yano, L.-W. Wang, N. S. Lewis, and H. A. Atwater, Bandgap tunability in Zn (Sn, Ge) N<sub>2</sub> semiconductor alloys, *Adv. Mater.* **26**, 1235 (2014).
- [54] W. Lü, D. B. Li, C. R. Li, and Z. Zhang, Generation and behavior of pure-edge threading misfit dislocations in In<sub>x</sub>Ga<sub>1-x</sub>N/GaN multiple quantum wells, *J. Appl. Phys.* **96**, 5267 (2004).

- [55] T. L. Song, Strain relaxation due to V-pit formation in  $\text{In}_x\text{Ga}_{1-x}\text{N}/\text{GaN}$  epilayers grown on sapphire, *J. Appl. Phys.* **98**, 084906 (2005).
- [56] S. Pereira, On the interpretation of structural and light emitting properties of InGaN/GaN epitaxial layers grown above and below the critical layer thickness, *Thin Solid Films* **515**, 164 (2006).
- [57] M. Cardona and P. Y. Yu, *Fundamentals of Semiconductors* Vol. 619 (Springer, Heidelberg, Germany, 2005).
- [58] C. Kittel and C.-y. Fong, *Quantum Theory of Solids* Vol. 5 (Wiley, New York, 1963).
- [59] J. M. Luttinger and W. Kohn, Motion of electrons and holes in perturbed periodic fields, *Phys. Rev.* **97**, 869 (1955).
- [60] E. P. O'Reilly, Valence band engineering in strained-layer structures, *Semicond. Sci. Technol.* **4**, 121 (1989).
- [61] Y. M. Sirenko, J.-B. Jeon, K. W. Kim, M. A. Littlejohn, and M. A. Stroscio, Strain effects on valence band structure in wurtzite GaN quantum wells, *Appl. Phys. Lett.* **69**, 2504 (1996).
- [62] G. L. Bir and G. E. Pikus, *Symmetry and Strain-Induced Effects in Semiconductors* Vol. 484 (Wiley, New York, 1974).
- [63] Q. Yan, P. Rinke, A. Janotti, M. Scheffler, and C. G. Van de Walle, Effects of strain on the band structure of group-III nitrides, *Phys. Rev. B* **90**, 125118 (2014).
- [64] P. Sengupta, H. Ryu, S. Lee, Y. Tan, and G. Klimeck, Numerical guidelines for setting up a k.p simulator with applications to quantum dot heterostructures and topological insulators, *J. Comput. Electron.* **15**, 115 (2016).
- [65] B. S. Eller, J. Yang, and R. J. Nemanich, Polarization effects of GaN and AlGaN: Polarization bound charge, band bending, and electronic surface states, *J. Electron. Mater.* **43**, 4560 (2014).
- [66] A. M. Shing, Y. Tolstova, N. S. Lewis, and H. A. Atwater, Growth of epitaxial  $\text{ZnSn}_x\text{Ge}_{1-x}\text{N}_2$  alloys by MBE, *Sci. Rep.* **7**, 1 (2017).
- [67] S. Lany, A. N. Fioretti, P. P. Zawadzki, L. T. Schelhas, E. S. Toberer, A. Zakutayev, and A. C. Tamboli, Monte Carlo simulations of disorder in  $\text{ZnSnN}_2$  and the effects on the electronic structure, *Phys. Rev. Mater.* **1**, 035401 (2017).
- [68] See the Supplemental Material at <http://link.aps.org/supplemental/10.1103/PhysRevApplied.18.064030> for the bulk and interface structures generated as a part of this study.
- [69] J. P. Perdew, K. Burke, and M. Ernzerhof, Generalized Gradient Approximation Made Simple, *Phys. Rev. Lett.* **77**, 3865 (1996).
- [70] S. L. Dudarev, G. A. Botton, S. Y. Savrasov, C. J. Humphreys, and A. P. Sutton, Electron-energy-loss spectra and the structural stability of nickel oxide: An LSDAU study, *Phys. Rev. B* **57**, 1505 (1998).
- [71] G. Kresse and D. Joubert, From ultrasoft pseudopotentials to the projector augmented-wave method, *Phys. Rev. B* **59**, 1758 (1999).
- [72] A. H. Larsen, J. J. Mortensen, J. Blomqvist, I. E. Castelli, R. Christensen, M. Dufak, J. Friis, M. N. Groves, B. Hammer, C. Hargus, *et al.*, The atomic simulation environment—a PYTHON library for working with atoms, *J. Phys.: Condens. Matter* **29**, 273002 (2017).
- [73] J. Paier, R. Hirschl, M. Marsman, and G. Kresse, The Perdew-Burke-Ernzerhof exchange-correlation functional applied to the G2-1 test set using a plane-wave basis set, *J. Chem. Phys.* **122**, 234102 (2005).
- [74] S. Lany and A. Zunger, Accurate prediction of defect properties in density functional supercell calculations, *Modell. Simul. Mater. Sci. Eng.* **17**, 084002 (2009).
- [75] Y. Le Page and P. Saxe, Symmetry-general least-squares extraction of elastic data for strained materials from *ab initio* calculations of stress, *Phys. Rev. B* **65**, 104104 (2002).
- [76] X. Wu, D. Vanderbilt, and D. R. Hamann, Systematic treatment of displacements, strains, and electric fields in density-functional perturbation theory, *Phys. Rev. B* **72**, 035105 (2005).